

## Supporting information

### **Disentangling the magnetic dimensionality of alleged magnetically isolated cuprate spin-ladder CuHpCl system. A long lasting issue**

J. Jornet-Somoza,<sup>a,b</sup> F. Cosi,<sup>a</sup> M. Fumanal,<sup>a</sup> M. Deumal<sup>a</sup>

<sup>a</sup> Secció Química Física, Dept. Ciència de Materials i Química Física & IQTCUB, Universitat de Barcelona, Martí i Franquès 1, E-08820, Barcelona

<sup>b</sup> Nano-Bio Spectroscopy Group and ETSF, Universidad del País Vasco, CFM CSIC-UPV/EHU, E-20018, San Sebastián

## Supporting Information Section 1

Nine different within-ladder d1-d9 pairs of radicals were selected according to the 14.00 Å threshold. The intra-ladder pairs of radicals are: (a) five d1-d5 nearest neighbors (**nn**) and (b) four d6-d9 next-nearest neighbors (**nnn**) radical pairs. Notice that, as the copper atoms are not perfectly aligned within a rail of the ladder, the Cu···Cu distance for “**nnn**” d9 pair (namely, 13.990 Å at  $T_{\text{room}}$ ) is slightly shorter than the sum of Cu···Cu distances for “**nn**” d3 and d5 pairs (namely, 6.996 Å + 7.002 Å = 13.998 Å). All selected d1-d9 radical intra-ladder pairs are shown in Figure S1.1, and schematically shown in main text Figure 1d.

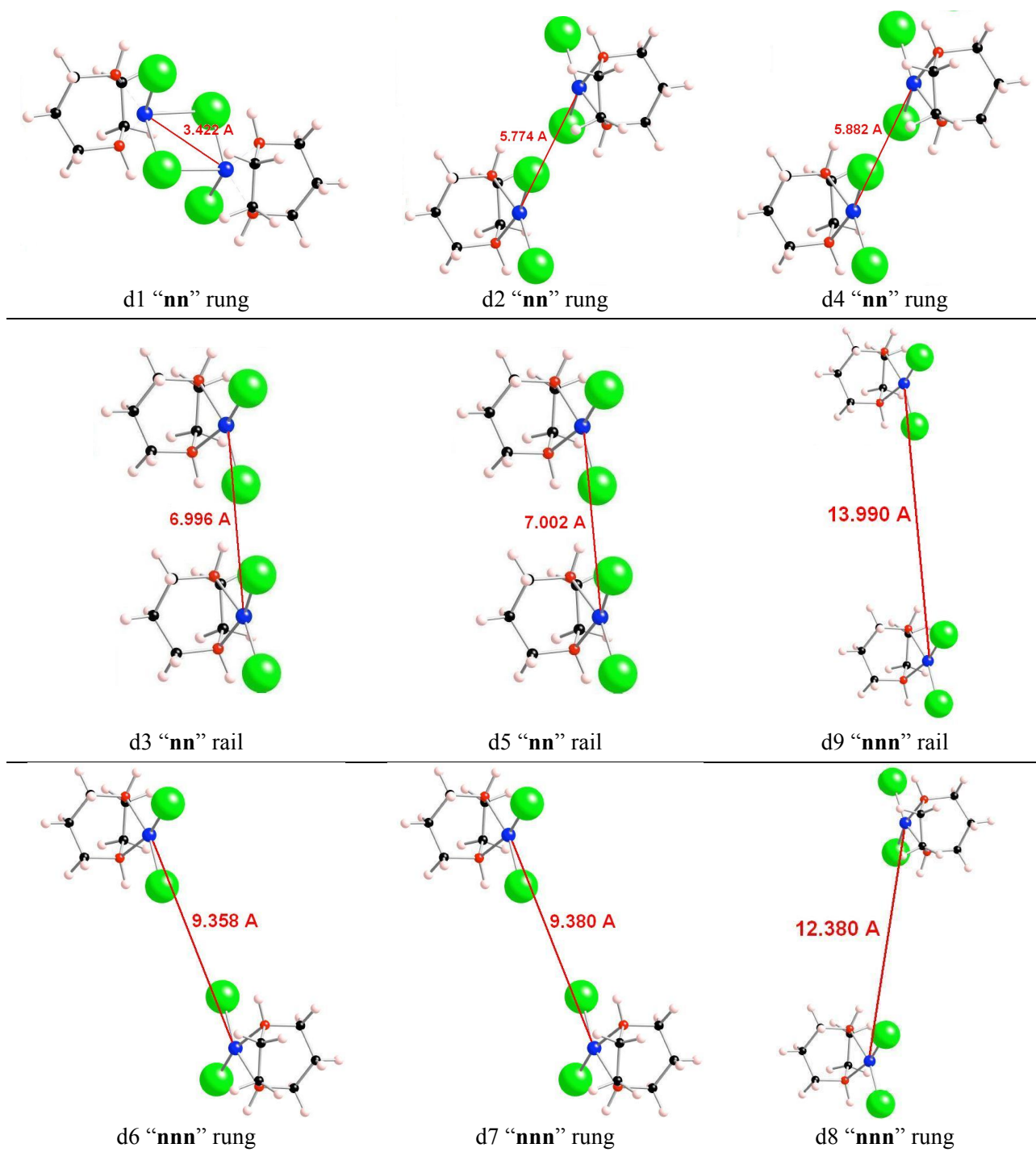


**Figure S1.1.** View of within ladder dimers. Each pair is classified in terms of being either “**nn**” (i.e. nearest neighbor) or “**nnn**” (i.e. next nearest neighbor) (see schematic representation in Figure 1d). The distances shown correspond to the crystal structure obtained at room temperature.

We also selected fifteen pairs of radicals arising from four *A-D* different spatial arrangements between ladders, which depend on the orientation between  $\text{Cu}_2(\text{C}_5\text{H}_{12}\text{N}_2)_2\text{Cl}_4$  moieties along either *a*- or *c*-axes (see highlighted atoms in yellow in Figures S1.2a-d, respectively).

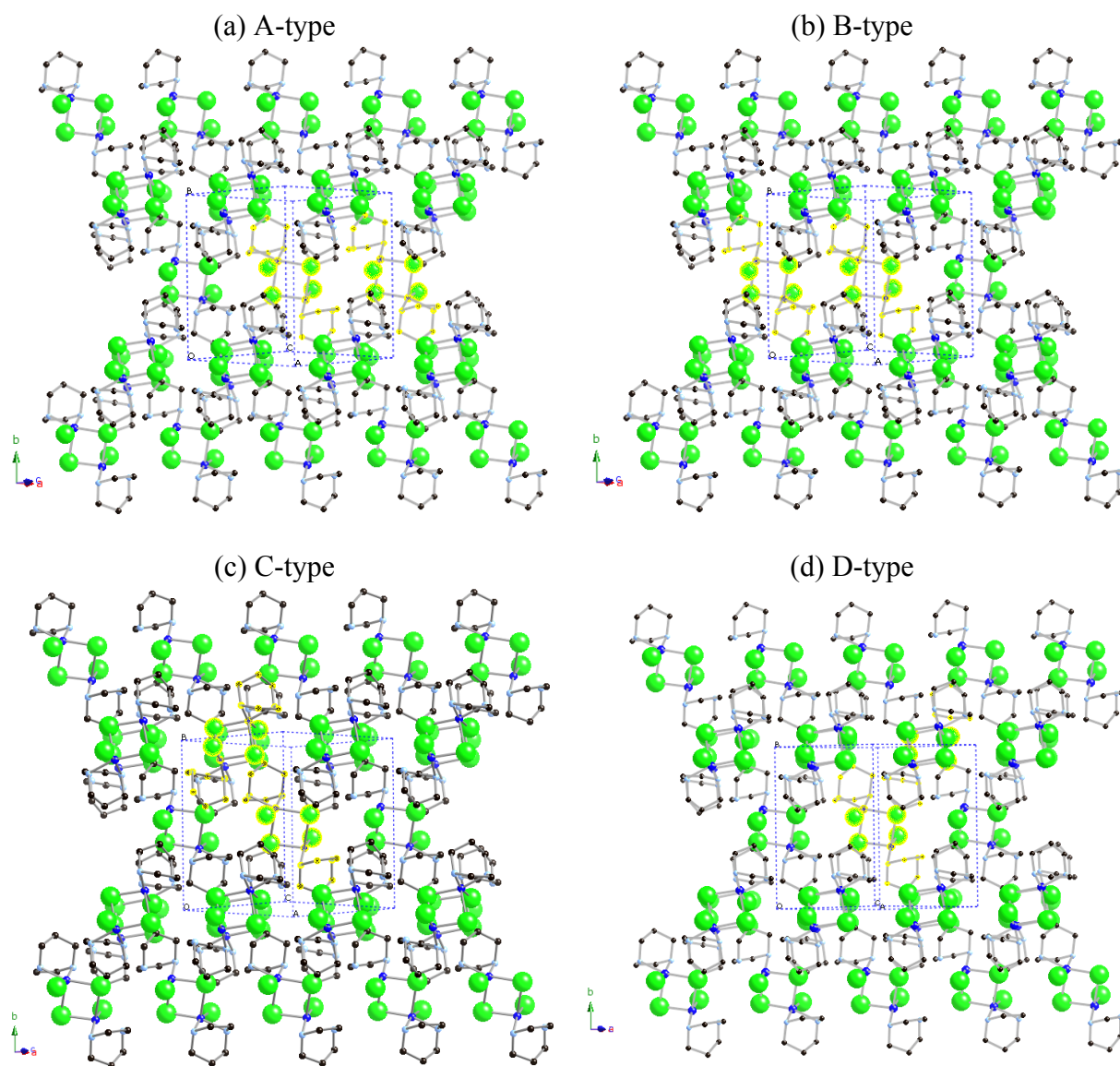


**Figure S1.2.** View along the *b*-axis of the four different spatial arrangements between ladders: (a) A-type, (b) B-type, (c) C-type, and (d) D-type. Each type is classified in terms of the orientation between  $\text{Cu}_2(\text{C}_5\text{H}_{12}\text{N}_2)_2\text{Cl}_4$  moieties along either *a*- or *c*-axes (see highlighted atoms in yellow). Notice that some atoms are omitted for clarity.

Dimers from the first spatial arrangement *A* are schematically illustrated in main text Figure 1e. All selected d10-d24 radical pairs are classified in terms of  $\text{Cu}\cdots\text{Cu}$  distances (see Figures S1.3-S1.4 for  $\text{Cu}\cdots\text{Cu}$  distances using the crystal structure at  $T_{\text{room}}$ ).

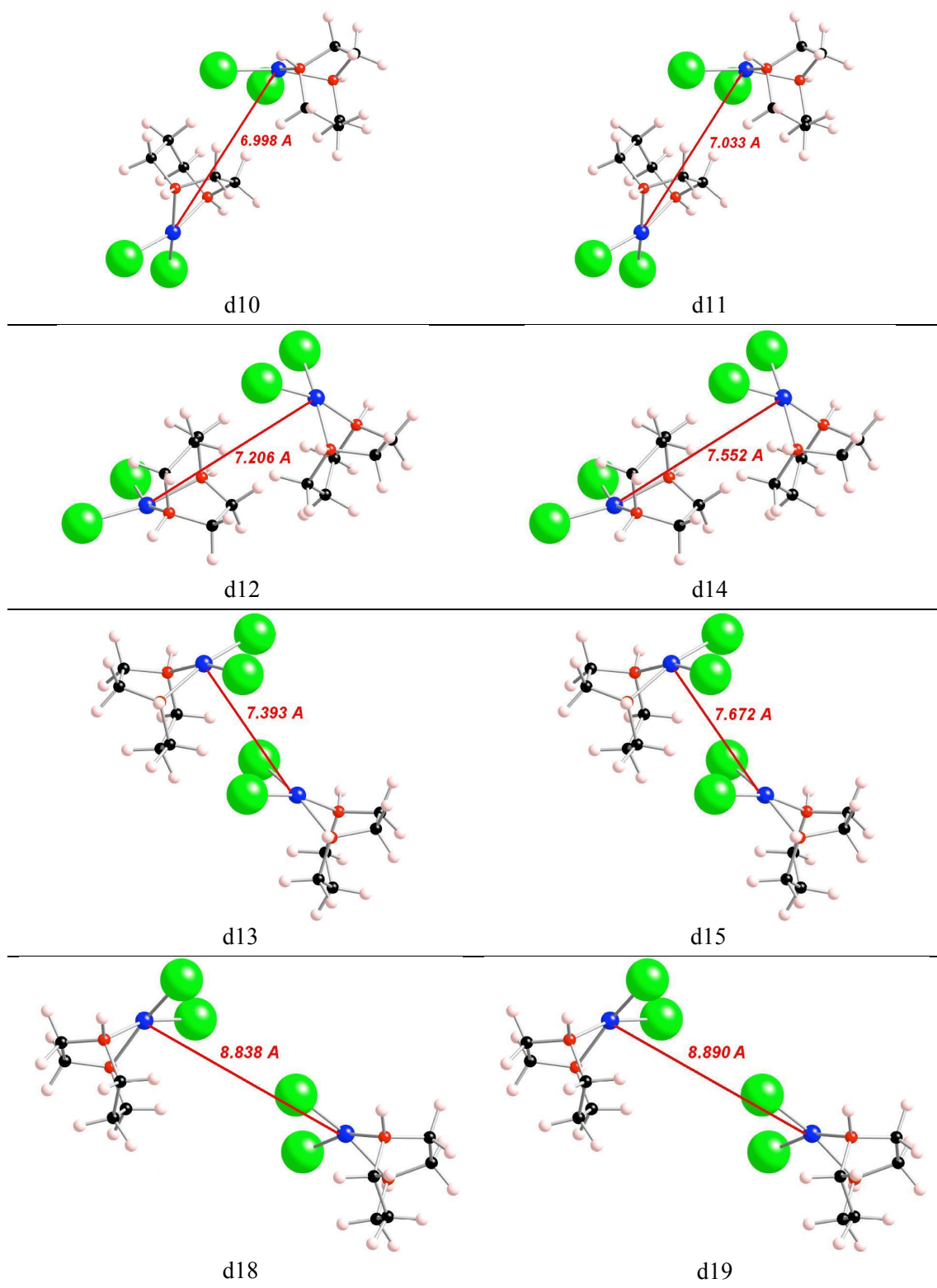


**Figure S1.3.** View of inter-ladder dimers from spatial arrangement *A* (d10, d11, d12, d14), and *B* (d13, d15, d18, d19). The distances shown correspond to the crystal structure obtained at room temperature.

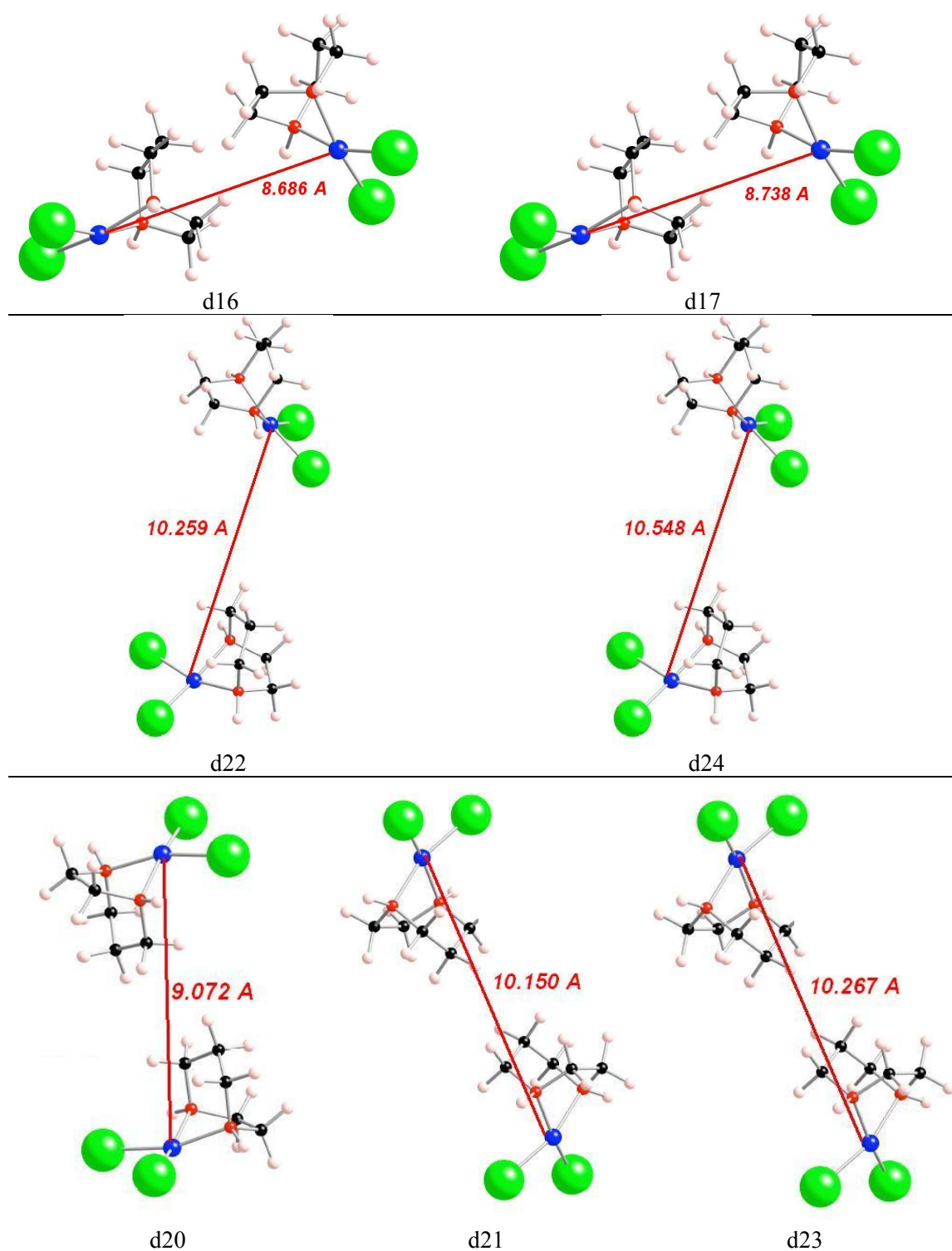


**Figure S1.4.** View of inter-ladder dimers from spatial arrangement C (d16, d17, d22, d24) and D (d20, d21, d23). The distances shown correspond to the crystal structure obtained at room temperature.

Table S1.1 shows the Cu $\cdots$ Cu distances (in Å) for both intra- and inter-ladder pairs of radicals that show a non-negligible magnetic coupling, once the corresponding  $J(\text{di})$  magnetic interaction has been computed using a tetramer cluster model. Complementarily, Table S1.2 gives the Cu $\cdots$ Cu distance and corresponding  $J(\text{di})$  value for each inter-ladder pair of radicals belonging to spatial arrangements *B-D* within the CuHpCl crystal packing.

**Table S1.1.** Cu···Cu distances in Å for d1-d7, d10-d12 and d14 obtained at **(a)** 4 K experimental crystal structure (from M.B. Stone, Y. Chen, J. Rittner, H. Yardimci, D.H. Reich, C. Broholm, D.V. Ferraris, and T. Lectka, *Phys. Rev. B*, 2002, **65**, 064423); and **(b)** room temperature experimental crystal structure (from B. Chiari, O. Piovesana, T. Tarantelli, and P.F. Zanazzi, *Inorg. Chem.*, 1990, **29**, 1172).

<b>di</b> pair of radicals	<b>(a)</b> 4 K	<b>(b)</b> T <sub>room</sub>
<b>d1</b>	3.376	3.422
<b>d2</b>	5.757	5.774
<b>d3</b>	6.987	6.996
<b>d4</b>	5.814	5.822
<b>d5</b>	7.000	7.002
<b>d6</b>	9.328	9.358
<b>d7</b>	9.344	9.380
<b>d10</b>	7.026	6.998
<b>d11</b>	7.059	7.033
<b>d12</b>	7.156	7.206
<b>d14</b>	7.504	7.552

**Table S1.2.** Cu···Cu distances for the room temperature crystal structure (in Å) and corresponding  $J(di)$  values (in cm<sup>-1</sup>) of selected radical pairs connecting two nearby spin-ladders classified according to the *B-D* different spatial arrangements identified in the Cu<sub>2</sub>(C<sub>5</sub>H<sub>12</sub>N<sub>2</sub>)<sub>2</sub>Cl<sub>4</sub> crystal.

Spatial arrangement <i>B</i>			Spatial arrangement <i>C</i>			Spatial arrangement <i>D</i>		
di	Cu···Cu /Å	$J(di)$ /cm <sup>-1</sup>	di	Cu···Cu /Å	$J(di)$ /cm <sup>-1</sup>	di	Cu···Cu /Å	$J(di)$ /cm <sup>-1</sup>
<b>d13</b>	7.393	0.02	<b>d16</b>	8.686	0.00	<b>d20</b>	9.072	0.07
<b>d15</b>	7.672	0.02	<b>d17</b>	8.758	0.00	<b>d21</b>	10.150	0.00
<b>d18</b>	8.838	0.00	<b>d22</b>	10.259	0.00	<b>d23</b>	10.267	-0.04
<b>d19</b>	8.890	0.00	<b>d24</b>	10.548	0.00			

## Supporting Information Section 2

The calculation of  $J(di)$  requires some detailed discussion. If only two radicals are involved (see Figure S2.1a for d3), there is only one  $J(di)$  that characterizes the magnetic interaction between them. The calculation of  $J(di)$  requires the evaluation of the open-shell broken-symmetry singlet (BS,S) and triplet (T) energies. In this case, for:

$$\hat{H} = -2 \sum_{A,B}^N J_{AB} \hat{S}_A \cdot \hat{S}_B$$

and  $S=1/2$  radicals with nearly zero overlap between SOMO orbitals,  $J(di) = E^{\text{BS,S}} - E^{\text{T}}$ . This is the procedure followed to obtain the  $J(di)$  value using a dimer model for both  $T_{\text{room}}$  and 4 K as listed in Table S2.1.

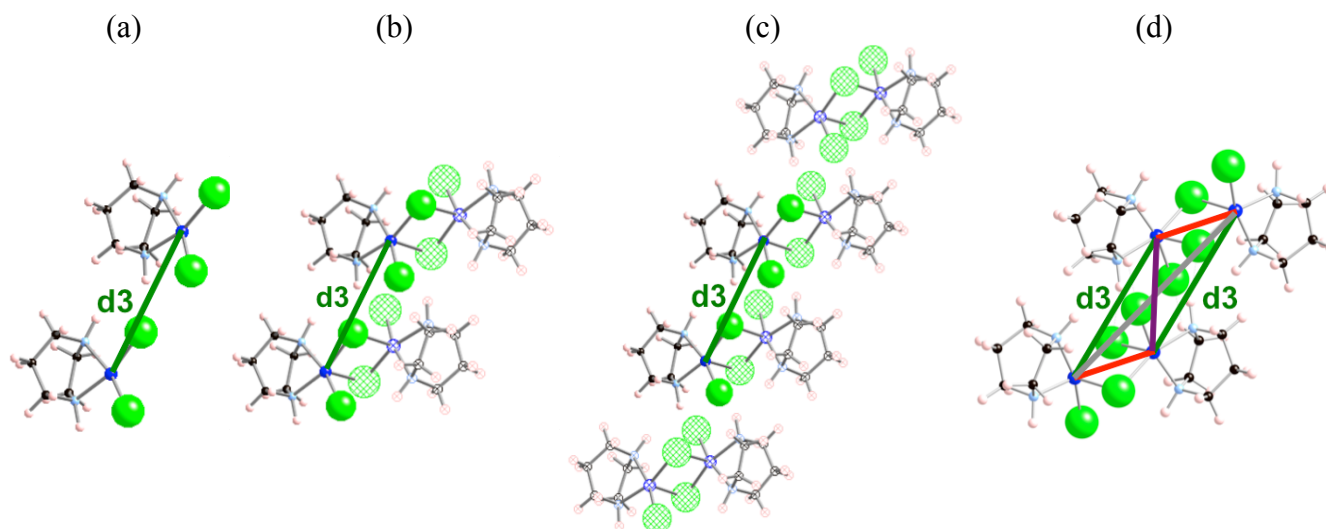


**Figure S2.1.** Evaluation of  $J(d3)$  (in green) using as a cluster model: (a) a bare d3 dimer, (b) a tetramer-based model that explicitly accounts for the radical d3 pair under study and the point charges of its d1 counterparts [dimer/d3-d1PC], (c) an eight radical model consisting on a two radical d3 pair embedded in six radicals represented by point charges [dimer/d3-d1PC]-4PC, and (d) a tetramer (where d1 in red, d2 in grey & d7 in purple).

**Table S2.1.** Magnetically non-negligible  $J(di)$  interactions (in  $\text{cm}^{-1}$ ) of selected radical pairs. Results using four different cluster models (namely, dimer, dimer with point charges and tetramer) for both intra- and inter-ladder  $J(di)$  are shown for the room temperature ( $T_{\text{room}}$ , HT) and 4K (LT) crystal structures. PC stands for point charges of a given radical pair. See Figure S2.1 for description of cluster models.

model	T	<i>intra-ladder</i>					<i>inter-ladder</i>			
		----- nn -----		--- nnn ---			<i>J(d10)</i>	<i>J(d11)</i>	<i>J(d12)</i>	<i>J(d14)</i>
dimer	$T_{\text{room}}$	+2.92	+2.39	-2.48	-0.97	-0.33	+0.31	-0.22	-1.16	-1.40
	4 K	+3.13	+2.11	-3.12	-	-	-	-	-1.27	-1.64
[dimer/di-d1PC]	4 K	+3.13 <sup>b</sup>	+0.08	-4.31	-1.08	-0.42	+0.23	-0.42	-1.10	-1.38
[dimer/di-d1PC]-4PC	4 K	+2.02	+0.28	-3.68						
tetramer	$T_{\text{room}}$	+2.37 <sup>a</sup>	-0.13	-3.58	-0.29	-0.13	+0.33	-0.11	-1.01	-1.19
	4 K	+2.30 <sup>a</sup>	-0.37	-3.88	-0.29	-0.12	+0.22	-0.31	-1.05	-1.38

<sup>a</sup> Average value using  $J(d1)$  resulting from the calculations to obtain  $J(d3)$  and  $J(d5)$  using a tetramer.

<sup>b</sup>  $J(d1)$  has been calculated with a modified dimer/d1-PC model which includes explicitly the d1 pair and the point charges of its nearest top and bottom d1 pairs, i.e. an hexamer model. See Figure S2.1 for models.

If four radicals are involved (see Figure S2.1d), there are (at least) 4 different  $J(di)$ 's among pairs of these four radicals. Therefore, the calculation of 4 different  $J(di)$ 's requires the evaluation of the energy of five different spin states. Within the tetramer approach, the spin states that have been evaluated are the high spin quintuplet (HS), two triplet (LS1, LS2) and two singlet (LS1/4, LS1/3) states. As an explicit example, Figure S2.2a-b shows how to obtain all  $J(di)$  interactions for two 'intra-ladder' models, and Figure S2.3 for an 'inter-ladder' model. This is thus the strategy followed to obtain the  $J(di)$  value using a tetramer model for both  $T_{room}$  and 4 K as listed in Table S2.1. Specifically Figure S2.2 shows the set of equations used to calculate the non-negligible intra-ladder magnetic interaction between CuHpCl radicals in dimers **d1**, **d3**, **d5**, **d6**, and **d7**. The inter-ladder significant magnetic interactions for radical dimers **d10**, **d11**, **d12**, and **d14** are obtained using the set of equations shown in Figure S2.3.

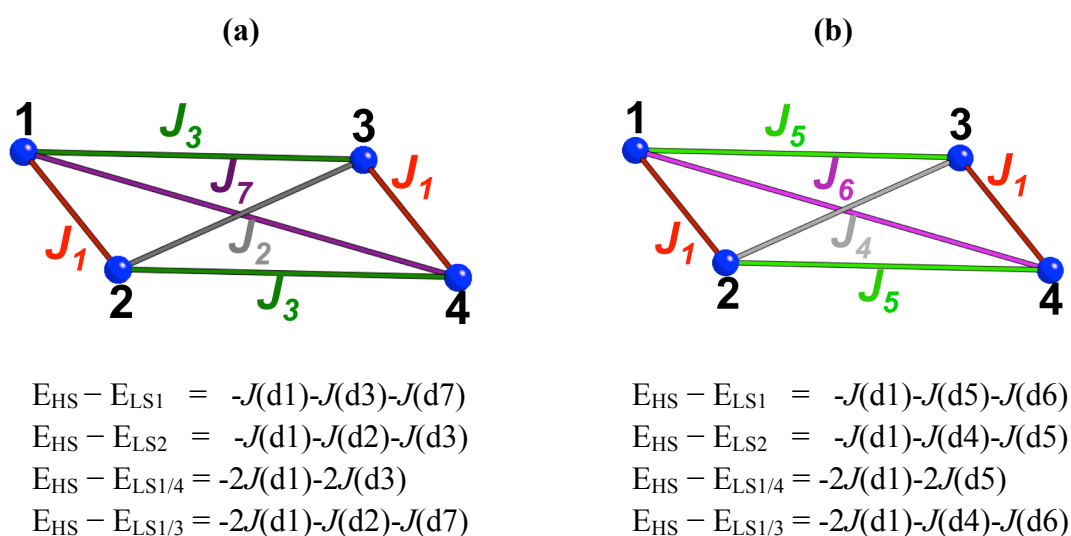


**Figure S2.2.** 'Intra-ladder' tetramer models used to obtain (a)  $J(d1)$ ,  $J(d2)$ ,  $J(d3)$ ,  $J(d7)$  and (b)  $J(d1)$ ,  $J(d4)$ ,  $J(d5)$ ,  $J(d6)$ .  $E_{LSij}$  indicates that a single beta spin is located in radicals ' $i/j$ ' (see radical numbering inset in model). Note that only Cu atoms are shown in the tetramer schemes for clarity.

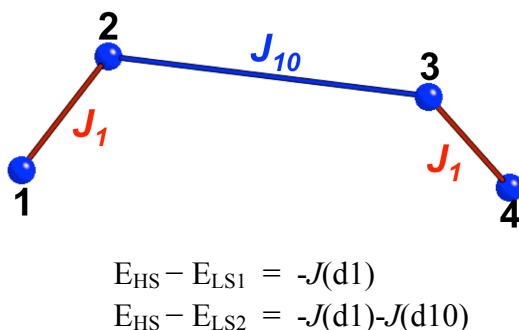


**Figure S2.3.** 'Inter-ladder' tetramer model used to obtain  $J(d10)$ ,  $J(d11)$ ,  $J(d12)$  and  $J(d14)$ .  $E_{LSi}$  indicates that a single beta spin is located in radicals ' $i$ ' (see radical numbering inset in model). Note that only Cu atoms are shown in the tetramer scheme for clarity.

So far, a 4-radical cluster model explicitly accounting for the two  $\text{Cu}_2(\text{C}_5\text{H}_{12}\text{N}_2)_2\text{Cl}_4$  units involved in any  $J(\text{di})$  under study has been used to compute all the  $\text{Cu}\cdots\text{Cu}$  magnetic interactions  $J(\text{di})$  (see tetramer model for d3 in Figure S2.1d). In order to assess its validity, two additional models have been considered, together with the bare  $\text{Cu}(\text{C}_5\text{H}_{12}\text{N}_2)\text{Cl}_2\cdots[\text{Cu}(\text{C}_5\text{H}_{12}\text{N}_2)\text{Cl}_2$  dimer di model (see Figure S2.1a). The first model is based again upon a tetramer, that consists of the radical pair to be studied and the point charges (PC) of the d1 radicals bonded to it (namely, [dimer/di-d1PC] in Figure S2.1b). The second model used considers eight radicals: two radicals are the specific dimer whose interaction one wants to evaluate and the remaining six radicals are represented by their point charges.<sup>[S2.1]</sup> Basically, the explicit dimer model is first connected through d1 to its  $\text{Cu}(\text{C}_5\text{H}_{12}\text{N}_2)\text{Cl}_2$  point charge counterpart, and then embedded in the point charges of 4 further surrounding Cu-based radicals (namely, [dimer/di-d1PC]-4PC in Figure S2.1c).

Let us consider the coupling between radicals giving rise to the d3 dimer pair. It is striking to realize that  $J(\text{d3})$  converts from weakly AFM ( $-0.37\text{ cm}^{-1}$ ) when it is evaluated according to a tetramer model to FM if the environment is not well described. Accordingly,  $J(\text{d3})$  is  $+0.08\text{ cm}^{-1}$  using the [dimer/d3-d1PC] model,  $+0.28\text{ cm}^{-1}$  using the [dimer/d3-d1PC]-4PC model, and  $+2.11\text{ cm}^{-1}$  with a bare d3 dimer model. The dependency on the model is not that critical for all remaining radical $\cdots$ radical  $J(\text{di})$  couplings. Yet, the  $J(\text{di})$  values computed with the tetramer model are the most reliable since the radical environment is best described.

---

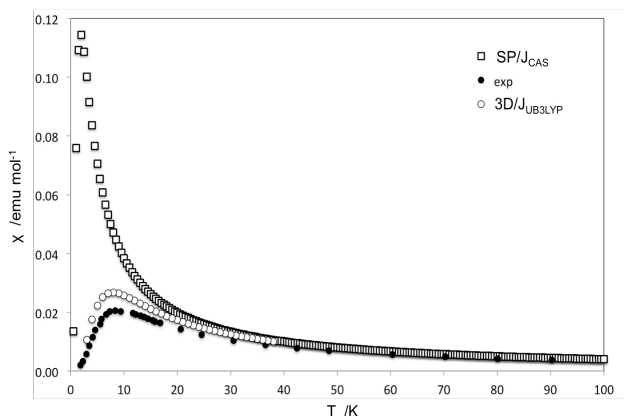
[S2.1] Electrostatic potential-derived charges according to the Merz-Singht-Kollman scheme: (a) B.H. Besler, K.M. Merz Jr., and P.A. Kollman, *J. Comp. Chem.*, 1990, **11**, 431; (b) U.C. Singh, and P.A. Kollman, *J. Comp. Chem.*, 1984, **5**, 129.

## Supporting Information Section 3

Given the relevance of the value of the calculated  $J(di)$  exchange interactions,  $J_{AB}$  couplings have been also calculated using the CASSCF wavefunction-based method. The results show that  $J(d3)^{CAS} = -0.15 \text{ cm}^{-1}$  and  $J(d5)^{CAS} = -1.03 \text{ cm}^{-1}$  are one order of magnitude different at CASSCF(6,6) level, which fully supports our DFT/UB3LYP calculations ( $-0.37 \text{ cm}^{-1}$  and  $-3.88 \text{ cm}^{-1}$ , respectively). Note that same basis sets have been used in UB3LYP and CASSCF calculations, namely the standard 6-31+G(d,p) for carbon, chlorine, hydrogen and nitrogen, and Ahlrich-pVDZ for copper.

Simulations of magnetic susceptibility  $\chi(T)$ , heat capacity  $C_p(T)$  and magnetization  $M(H)$  using a spin ladder as magnetic model (16 radicals) with the  $J_{AB}$  values obtained at CASSCF level (namely, SP/ $J_{CAS}$ :  $J(d1)^{CAS} = +0.62 \text{ cm}^{-1}$ ;  $J(d3)^{CAS} = -0.15 \text{ cm}^{-1}$ ;  $J(d5)^{CAS} = -1.03 \text{ cm}^{-1}$ ) show no agreement with experimental data (see empty square symbols in Figure S3.1a for  $\chi(T)$ , Figure S3.1b for  $C_p(T)$ , and Figure S3.2a-b for  $M(H)$ ). In fact, for SP/ $J_{CAS}$ , not only the calculated  $dM/dH(H)$  data (Figure S3.2a) do not resemble its experimental counterpart signature to extract  $H_{c1}$  and  $H_{c2}$  values, but also there is a *ca.* 6.0 T shift when comparing calculated and experimental  $M/M_{sat}$  data as a function of the magnetic field,  $H$  (Figure S3.2b). Note that here  $M_{sat}$  is the saturated value of the magnetization. It is indeed the calculated data using a 3D magnetic model (16 radicals) with the  $J_{AB}$  values at UB3LYP level (3D/ $J_{UB3LYP}$ :  $J(d1) = +2.30 \text{ cm}^{-1}$ ;  $J(d3) = -0.37 \text{ cm}^{-1}$ ;  $J(d5) = -3.88 \text{ cm}^{-1}$ ) that show good performance compared to experiment for both  $dM/dH$  and  $M/M_{sat}$  representations (see Figures S3.3a and S3.3b, respectively). Notice that Figures S3.3a-b display magnetization data as a function of the singlet-triplet gap with zero applied field,  $\Delta$ , which corresponds to  $H_{c1}$ . This representation has been chosen to highlight the good agreement between experimental and calculated magnetization data.

(a) magnetic susceptibility



(b) heat capacity

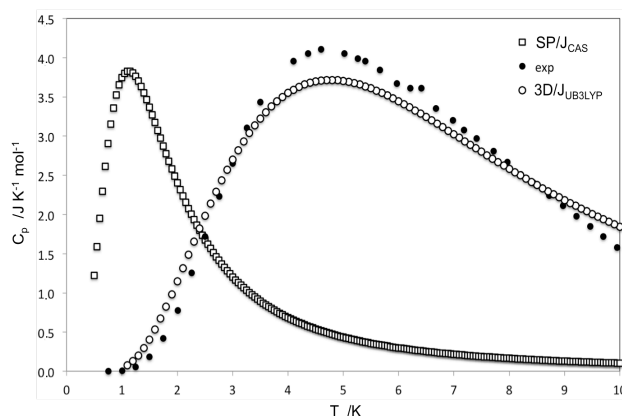
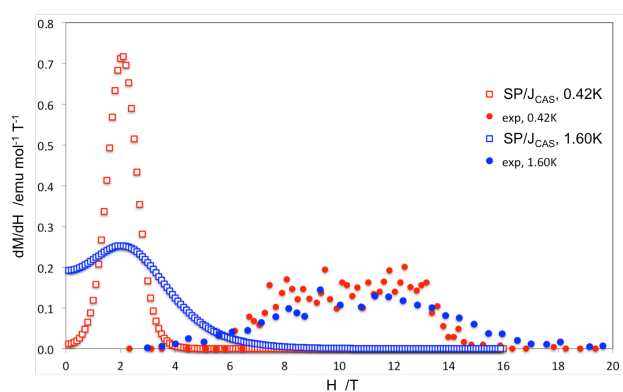


**Figure S3.1.** Comparison between experimental data (full black circle) and calculated data using a 16-radical spin ladder model with  $J(di)$  at CASSCF level (namely SP/ $J_{CAS}$ , empty squares) and a 3D model (16-radicals) with  $J(di)$  at UB3LYP level (namely SP/ $J_{UB3LYP}$ , empty circles) for (a) magnetic susceptibility and (b) heat capacity.

(a)  $dM/dH$  (using SP/ $J_{CAS}$ )



(b) magnetization as  $M/M_{\text{sat}}$  (using SP/ $J_{CAS}$ )

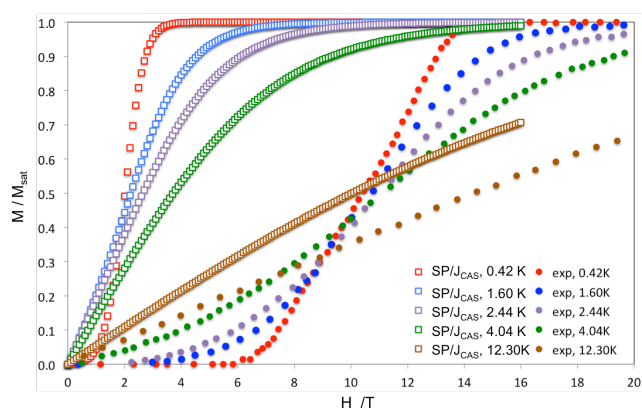
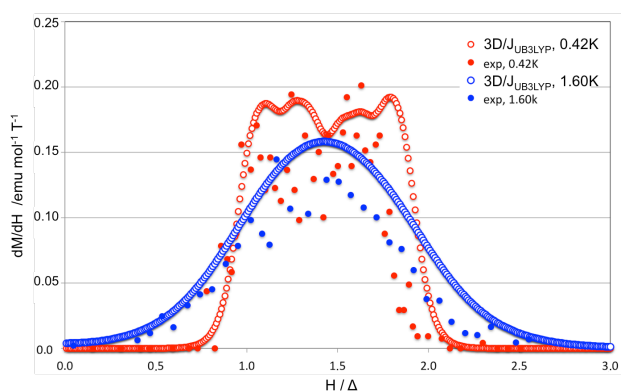


**Figure S3.2.** Comparison between experimental data (full circle) and calculated data at different temperatures using a 16-radical spin ladder model with  $J(\text{di})$  at CASSCF level (namely SP/ $J_{CAS}$ , empty squares) for (a)  $dM/dH(H)$  and (b)  $M/M_{\text{sat}}(H)$ . Note that  $M_{\text{sat}}$  is the saturated value of the magnetization.

(a)  $dM/dH$  (using SP/ $J_{UB3LYP}$ )



(b) magnetization as  $M/M_{\text{sat}}$  (using SP/ $J_{UB3LYP}$ )

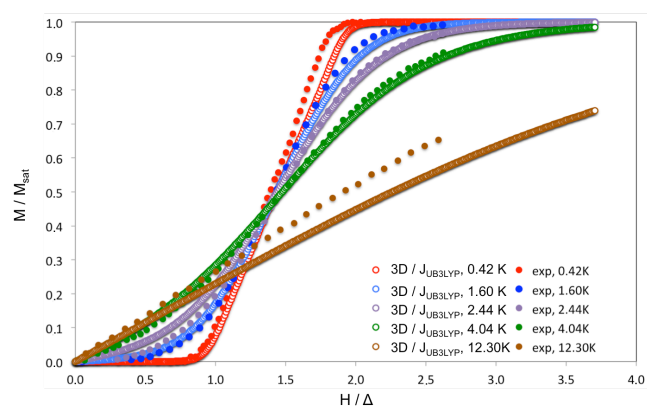


**Figure S3.3.** Comparison between experimental data (full circle) and calculated data at different temperatures using a 3D model (16-radicals) with  $J(\text{di})$  at UB3LYP level (namely SP/ $J_{UB3LYP}$ , empty circles) for (a)  $dM/dH$  and (b)  $M/M_{\text{sat}}$  as a function of the reduced magnetic field ( $H/\Delta$ ). Note that  $M_{\text{sat}}$  is the saturated value of the magnetization.

## Supporting Information Section 4

SI Section 2 has already addressed the importance of the cluster model to extract the  $J(\text{di})$  magnetic coupling between two CuHpCl radicals. It has been concluded that a tetramer model is more reliable since the radical environment is best described. At this level of modeling, the magnetic interactions  $J(\text{d3})$  and  $J(\text{d5})$  have remarkably different magnitude but a very similar geometry (see Figure S4.1a for overlap of radical pairs).

This apparent similarity does not hold when analyzing the atomic charges<sup>[S4.1a]</sup> of the Cl $\cdots$ H-N atoms involved in channeling the magnetic coupling for d3 and d5 (namely, Cl21 $\cdots$ H36N84 and Cl22 $\cdots$ H35N83 in Figure S4.1b). According to Table S4.1, it is possible to observe that there is a larger charge polarization of the atoms channeling the magnetic interaction for d3 than for d5, which can be taken as a signature for a larger degree of hydrogen bonding in d3. It is interesting to realize that the same conclusion is reached irrespective of using CM5<sup>[S4.2]</sup>, Hirshfeld<sup>[S4.3]</sup> or Mulliken<sup>[S4.4]</sup> schemes to calculate atomic charges, namely, charges in the atoms interacting via a hydrogen bond in d3 are larger than in d5. It must be also stressed that the value of the CM5 atomic charges is more consistent with reality, and will be used in main text Table 3. The fact that hydrogen bonding enhances FM exchange coupling between radicals has previously been encountered and documented.<sup>[S4.5]</sup> Note that, academically, hydrogen bonding is defined as an intermolecular force that forms a special type of dipole-dipole attraction when a hydrogen atom bonded to a strongly electronegative atom exists in the vicinity of another electronegative atom with a lone pair of electrons. Usually the electronegative atom is oxygen, nitrogen, or fluorine, which has a partial negative charge. The hydrogen then has the partial positive charge. Accordingly, the more polarized the hydrogen atoms are (i.e. the larger their partial positive charge is), the stronger the hydrogen bond is (see orange arrows in schematic representation in Figure S4.2). It follows that a less AFM  $J_{AB}$  value should be thus expected for radical pairs with a larger contribution from hydrogen bonding as realized in CuHpCl ( $J(\text{d3}) = -0.37 \text{ cm}^{-1}$  vs.  $J(\text{d5}) = -3.88 \text{ cm}^{-1}$ ).

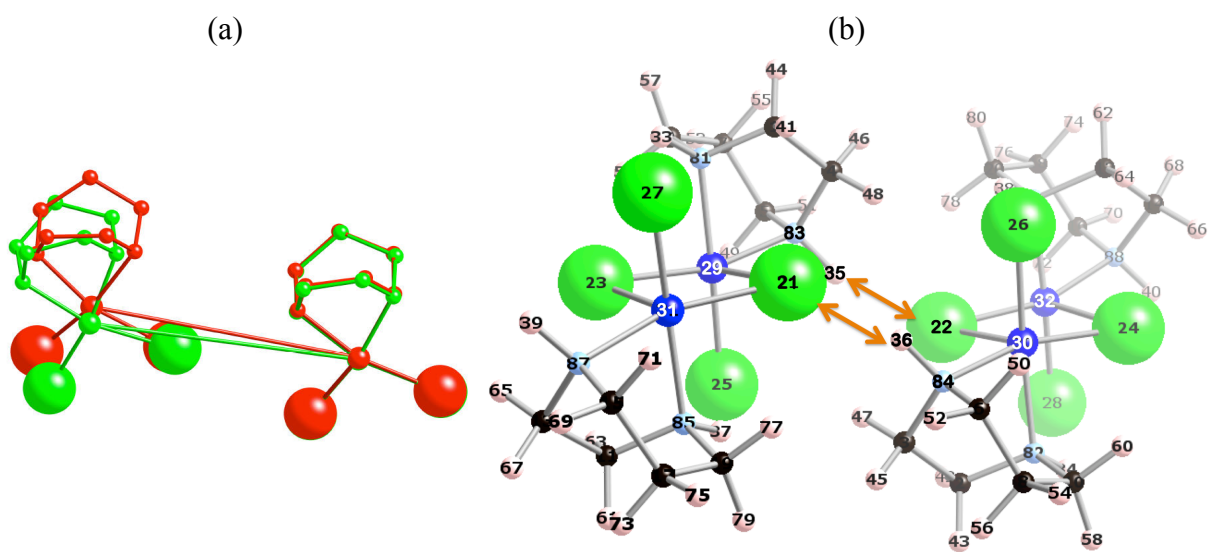
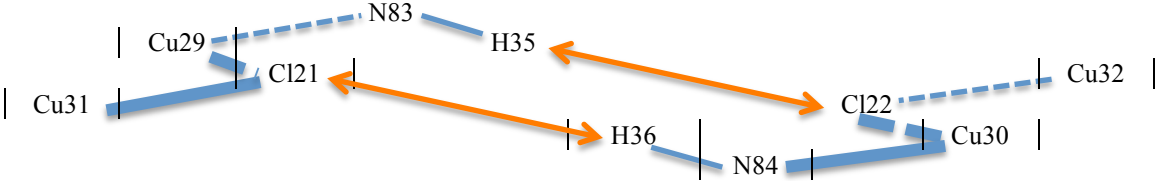


**Figure S4.1** (a) Overlap of d3 and d5 pairs of radicals (red and green, respectively) using a dimer model. (b) Representation of Cu-Cl $\cdots$ H-N magnetic channel in d3 / d5 using either a tetramer cluster model.

**Table S4.1.** Atomic charges according to CM5, Hirshfeld and Mulliken schemes for Cu-Cl...H-N magnetic channel in the d3 and d5 pairs of radicals. Spin density at Hirshfeld level is also given. Note that the atom numbering is in accordance with Figure S4.1b.



charge CM5									
d3	0.4702	0.4707	-0.3013		+0.2908	-0.5566		0.4706	0.4698
d5	0.4675	0.4735	-0.2877		+0.2898	-0.5515		0.4738	0.4678
charge Hirshfeld									
d3	0.4069	0.4081	-0.3468		+0.1197	-0.1299		0.4081	0.4069
d5	0.4047	0.4108	-0.3358		+0.1177	-0.1304		0.4108	0.4048
charge Mulliken									
d3	0.3536	0.1004	-0.3888		+0.4518	-0.4213		0.3536	0.3684
d5	0.3684	0.0400	-0.0616		+0.4473	-0.2942		0.1004	0.0400
spin density Hirshfeld									
d3	0.5733	0.5733	0.084		0.0044	0.0955		0.5733	0.5791
d5	0.5718	0.5808	0.090		0.0049	0.1007		0.5808	0.5718

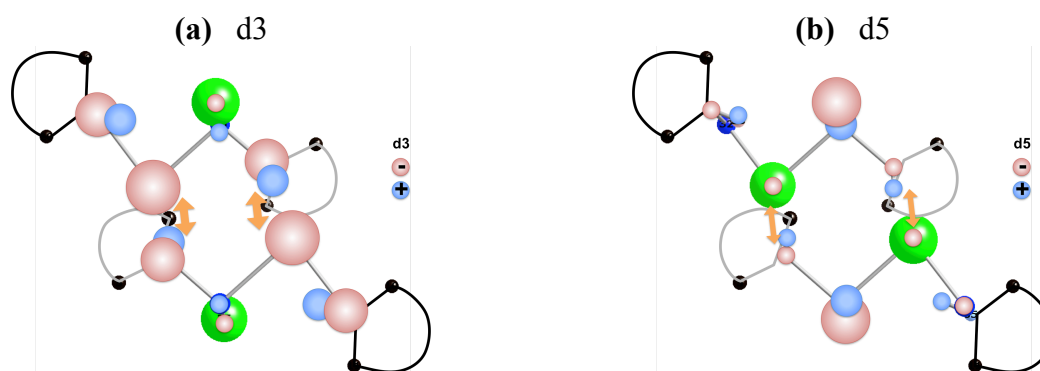


**Figure S4.2** Scheme to picture the relation between the strength of a hydrogen bond and the charge polarization of the atoms involved in (a) d3 and (b) d5. Color code: negative charge in pale red; positive charge in pale blue; Cl in light green; H in light pink; N in light blue; Cu in blue; C in black.

In addition, we have also analyzed the spin density<sup>[S4.3]</sup> along the Cu-Cl...H-N-Cu path which couples Cu(C<sub>5</sub>H<sub>12</sub>N<sub>2</sub>)Cl<sub>2</sub> radicals (see Table S4.1). Note that H36 of d3, which carries the largest partial charge, has smaller spin density than H36 of d5, as expected since hydrogen bonding in d3 is stronger than in d5. According to calculations, the spin density is larger in d5 and, in turn, the interaction  $J(d5)$  is more strongly AFM.

[S4.1] (a) Charge Model 5, CM5: (a) A.V. Marenich, S.V. Jerome, C.J. Cramer, and D.G. Truhlar, *J. Chem. Theory and Comput.* 2012, **8**, 527. Hirshfeld spin density: (b) F.L. Hirshfeld, *Theor. Chem. Acc.*, 1977, **44**, 129-38. (c) J. P. Ritchie and S. M. Bachrach, *J. Comp. Chem.*, 1987, **8**, 499.

[S4.2] A.V. Marenich, S.V. Jerome, C.J. Cramer, and D.G. Truhlar, *J. Chem. Theory and Comput.* 2012, **8**, 527

[S4.3] (a) F.L. Hirshfeld, *Theor. Chem. Acc.*, 1977, **44**, 129. (b) J.P. Ritchie and S.M. Bachrach, *J. Comp. Chem.*, 1987, **8**, 499

[S4.4] R. S. Mulliken, *J. Chem. Phys.* 1955, **23**, 1833

[S4.5] (a) F. M. Romero, R. Ziessel, M. Bonnet, Y. Pontillon, E. Ressouche, J. Schweizer, B. Delley, A. Grand, and C. Paulsen, *J. Am. Chem. Soc.*, 2000, **122**, 1298. (b) D. MasPOCH, L. Catala, P. Gerbier, D. Ruiz-Molina, J. Vidal-Gancedo, K. Wurst, C. Rovira, and J. Veciana, *Chem. Eur. J.*, 2002, **8**, 3635. (c) J. Choi, J.D. Woodward, J.L. Musfeldt, C.P. Landee, and M.M. Turnbull, *Chem. Mater.*, 2003, **15**, 2797. (d) S. Vela, J. Jornet-Somoza, M.M. Turnbull, R. Feyerherm, J.J. Novoa, and M. Deumal, *Inorg. Chem.*, 2013, **52**, 12923.

## Supporting Information Section 5

In order to compare our results with those reported in the literature, we studied the magnetic topology in terms of an isolated ladder model and, then, as a 3D model of interacting ladders. The first aim was, thus, to account for intra-ladder  $J_{AB}$  interactions, neglecting  $J(d10, d11, d12, d14)$  interactions (see Figure S5.1a). This model has been widely used in the literature but always neglecting the  $J_{rail}$  alternation. The second model chosen accounted for inter-ladder  $J_{AB}$  interactions and provided original results. This proposed model presents two 2-rung ladders that directly interact with one 4-rung ladder such that two inter-ladder  $J(d10, d11, 12, d14)$  set of interactions are taken into account (see Figure S5.1b).

The results obtained are compared with the experimental behavior reported by Hagiwara et al.<sup>[S5.1]</sup> (black line, Figure S5.1c). It is observed that, although both cases behave antiferromagnetically (AFM) and the calculated magnetic susceptibility values reproduce the experimental data at high temperature ( $>60\text{K}$ ), its intensity is overestimated. In fact, the calculated  $\chi(T)$  shows a maximum value at 4.5 K rather than 8 K and its numerical value has an error larger than 100% with respect to the experimental data. Besides, the spin gap using cyclic spin-ladder magnetic topology based on  $J_{AB}$  values obtained from dimer models is  $2.6\text{ cm}^{-1}$ , which differs from experimentally determined ( $7.5, 4.7$  and  $6.4\text{ cm}^{-1}$ ) and simulated using  $J_{AB}$  values obtained from tetramer models ( $5.4\text{ cm}^{-1}$ ). It is clear that the dimer-based model does not provide an adequate description.

The magnetic susceptibility  $\chi(T)$  curve has been simulated considering the  $J(\text{di})$  values obtained by means of the tetramer approach with a gyromagnetic  $g$  factor set to be 2.08 using two squared plaquette-based 3D models. Within the plaquette framework (see Figure S5.2a for magnetic building block), the magnetic models contemplated enable magnetic building blocks interact through antiferromagnetic (AFM)  $J(d12)$  and  $J(d14)$  interactions (Figures S5.2b-c).

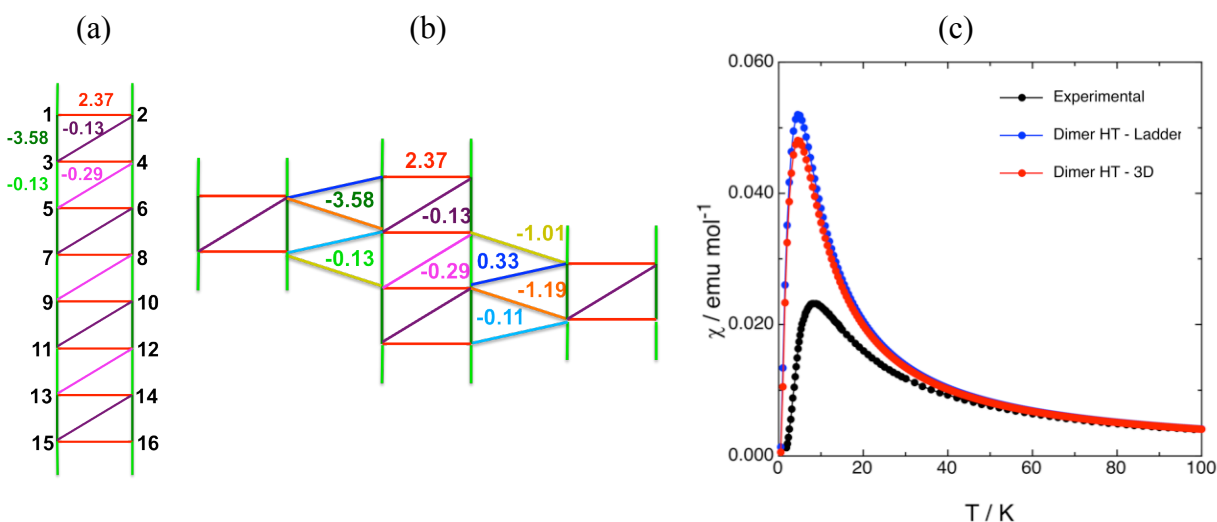


**Figure S5.1.** Ladder-based models: (a) isolated ladder model, and (b) interacting-ladder model proposed to account for the 3D magnetic topology of the CuHpCl crystal.  $J_{AB}$  values in  $\text{cm}^{-1}$ . The  $J(\text{di})$  indicated correspond to the tetramer cluster approach for the room temperature structure. (c) Simulated magnetic susceptibility  $\chi(T)$  data using an isolated ladder and 3D interacting ladder models.

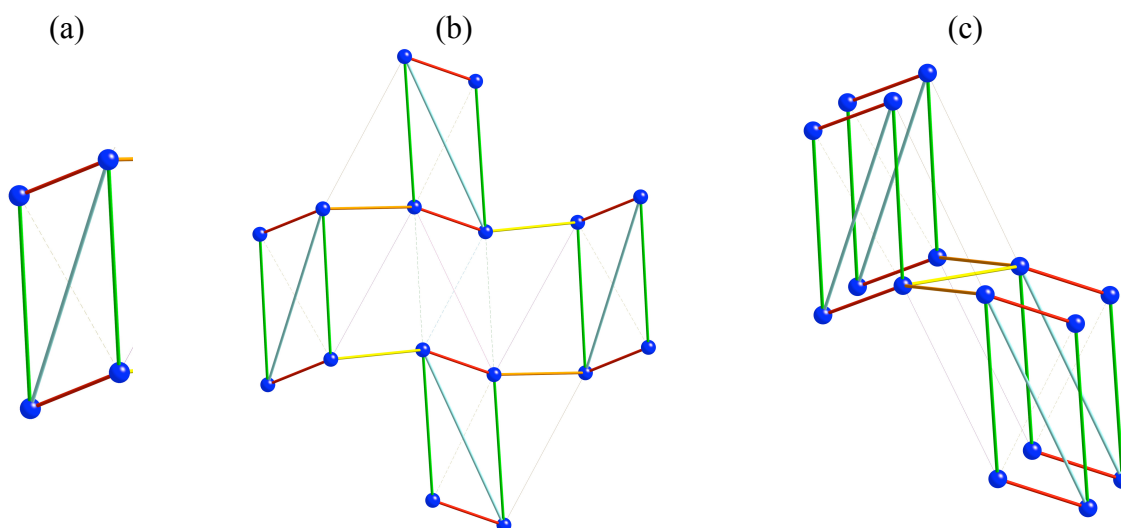


**Figure S5.2.** Plaquette-based models: (a) isolated squared plaquette magnetic building block model with  $J(d1)$ ,  $J(d5)$  and  $J(d6)$  exchange coupling interactions; (b) and (c) two different 3D models consisting in plaquette magnetic building blocks connected through  $J(d12)$  and  $J(d14)$ .

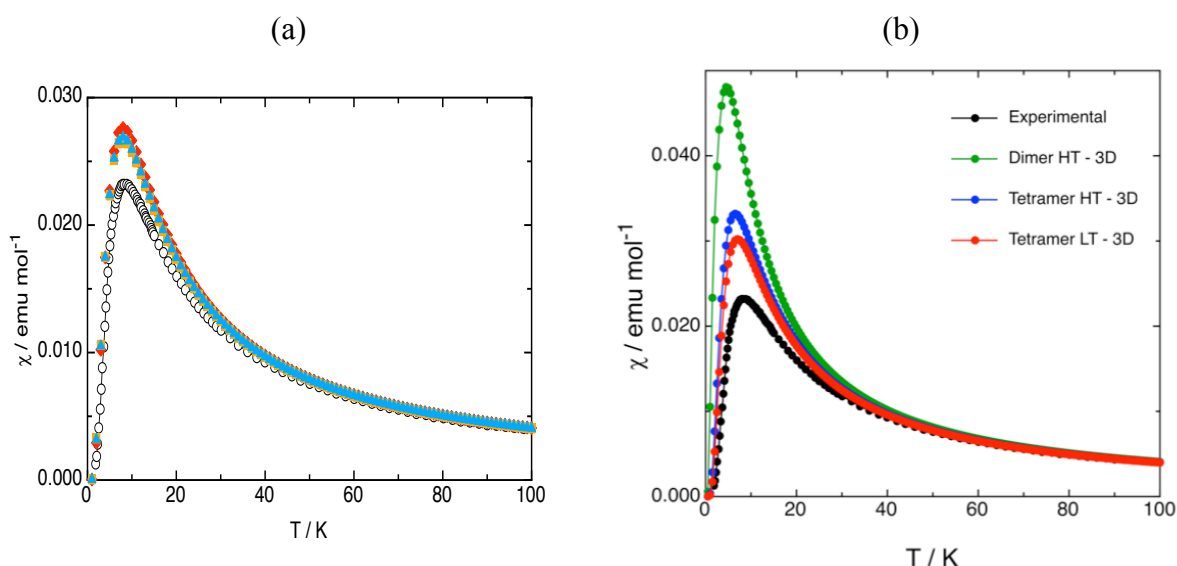


**Figure S5.3.** Magnetic susceptibility curves for: (a) plaquette-based models using  $J_{AB}$  values obtained by the tetramer approach at 4 K crystal structure (LT, model S5.2b in blue, and S5.2c in red), (b) 3D plaquette model using  $J_{AB}$  values obtained by the tetramer approach at room temperature (HT) and 4 K (LT) compared to 3D ladder models using  $J_{AB}$  values obtained by the dimer approach at HT.

Comparison of calculated  $\chi(T)$  with the experimental measurements (see Figure S5.3a) shows good agreement. The intensity of the peak reaches  $0.035 \text{ emu mol}^{-1}$  and appears at 6.5 K, which is a value close to the experimental 8 K. As discussed in the main text, the magnetic topology is not affected by temperature: it is the magnitude of the magnetic exchange values that is slightly influenced by the thermal contraction. Note that the calculated and experimental magnetic susceptibility data perfectly agree at high temperature ( $>60\text{K}$ ).

Further, if the magnetic susceptibility is calculated using the  $J(di)$  exchange values obtained with a bare dimer radical pair model with either the same 3D magnetic model of interacting squared plaquettes (see Tetramer HT/LT-3D in Figure S5.3b) or ladders (see Dimer HT-3D in Figure S5.3b), the resulting  $\chi(T)$  further supports the fact that the dimer cluster model does not provide an adequate description of the electronic environment to quantitatively compute  $J(di)$  magnetic interactions.

Finally, let us comment on the fact that the magnetization data is very sensitive to the magnetic model one uses to simulate it. In order to illustrate the very different response in magnetization we have selected the models displayed in Figure S5.4. Model 3Dm1 is the three-dimensional (3D) minimal magnetic model used to reproduce the experimental magnetic response of CuHpCl in this paper (see Figure S5.2b). We have then selected two other 3D models (3Dm2, 3Dm3) that do not account correctly for the magnetic topology of the material. Last, we have considered a hypothetical spin-ladder model (hypotheticalSP) and a quasi spin-ladder model (QSP). Notice that all models used contain 16 radicals and the corresponding  $J_{AB}$  coupling interactions are those calculated at 4 K.

As observed in Figure S5.5a, using the isotropic spin ladder magnetic model for simulation purposes, the shape of calculated  $M(H)$  (see turquoise symbols and model) is not compatible with the experimental data (black symbols). Calculated  $M(H)$  using the quasi spin ladder model

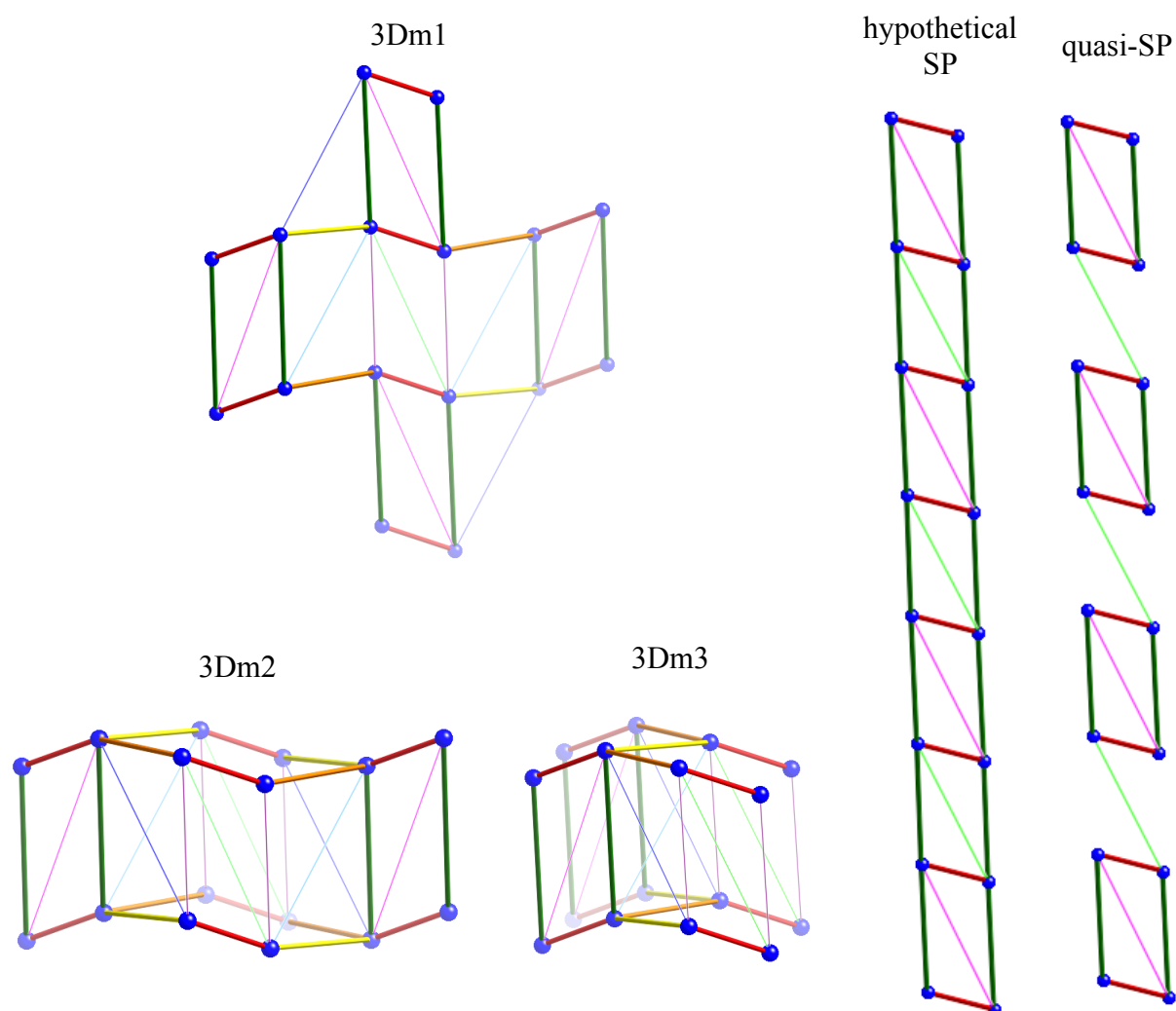


**Figure S5.4.** Magnetic models used to show that the magnetization data is very sensitive to the model used for simulation purposes. Color code:  $J(d1)$  in red ( $+2.30 \text{ cm}^{-1}$ );  $J(d5)$  in deep green ( $-3.88 \text{ cm}^{-1}$ );  $J(d12)$  in yellow ( $-1.05 \text{ cm}^{-1}$ );  $J(d14)$  in orange ( $-1.38 \text{ cm}^{-1}$ );  $J(d3)$  in purple ( $-0.37 \text{ cm}^{-1}$ );  $J(d6)$  in magenta ( $-0.29 \text{ cm}^{-1}$ );  $J(d7)$  in light green ( $-0.12 \text{ cm}^{-1}$ );  $J(d10)$  in deep blue ( $+0.22 \text{ cm}^{-1}$ );  $J(d11)$  in light blue ( $-0.31 \text{ cm}^{-1}$ ).

(see orange symbols and model) performs better but this performance is an artifact of the magnetic model. Here one has to realize that the quasi spin ladder model is basically a  $\pi$ -stack of four plaquettes (see Figure S5.5b for 3D magnetic model based on four connected plaquettes (highlighted in blue) and for the quasi spin ladder model (highlighted in orange). At this point, a reminder is in order: a plaquette which is defined by FM  $J(d1)$  and AFM  $J(d5)$  was identified as the magnetic building block of CuHpCl. Therefore, the quasi spin ladder model corresponds basically to four almost isolated plaquettes (since the inter-plaquette interaction is very weak, see Figure S5.5b). Comparison between calculated  $M(H)$  using this model (in orange) and the 3D interacting plaquette model (in blue) shows that it is required to connect the plaquettes through  $J(d12)$  and  $J(14)$  to obtain a better accuracy of the  $M(H)$  data ranging from  $M/M_{\text{sat}}$  0.4 to 0.7 (highlighted in lime green in Figure S5.5a). Note that, using the quasi spin ladder (in orange),  $M(H)$  has a plateau in this region, which is not exhibited by the experimental data (and neither by the 3D interacting plaquettes model). It thus corroborates the validity of the magnetic model used for simulation purposes.

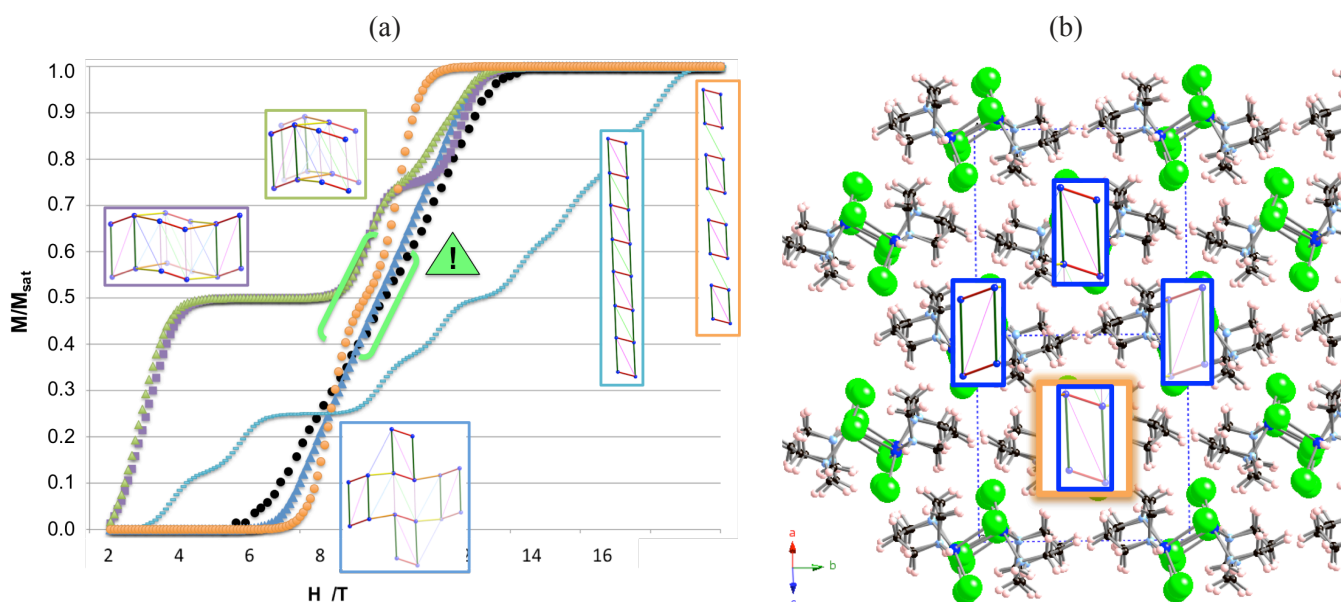


**Figure S5.5.** (a) Magnetization data using the different models shown in Figure S4.4 expressed in terms of its saturation value. Color code: 3Dm1 in blue; 3Dm2 in purple; 3Dm3 in green; hypothetical spin-ladder SP in turquoise; quasi-spin-ladder QSP in orange; experimental in black. Note experimental data has been shifted by 2.7 T for comparison reasons (see further discussion in next SI Section 6). (b) View along the  $\pi$ -stacking to better realize the magnetic models: 3D (in blue, 3Dm1) and quasi spin ladder (in orange, QSP).

[S5.1] M. Hagiwara, Y. Narumi, K. Kindo, T. Nishida, M. Kaburagi, and T. Tonegawa, *Physica B*, 1998, **246-247**, 234

## Supporting Information Section 6

The inflection points in  $dM/dH$  show where the critical fields appear (see Figure S6.1a). From the lowest temperature  $M(H)$  curve at 0.42 K (Figure S6.1b), our data agree with a nonmagnetic solid below 5.2 T ( $H_{c1,exp} = 7.4 \pm 0.1$  T) in a singlet ground state, whose magnetization remains zero. With increasing field, the magnetization increases until it reaches its saturation value at 10.4 T ( $H_{c2,exp} = 13.2 \pm 0.3$  T), above which CuHpCl is fully polarized.

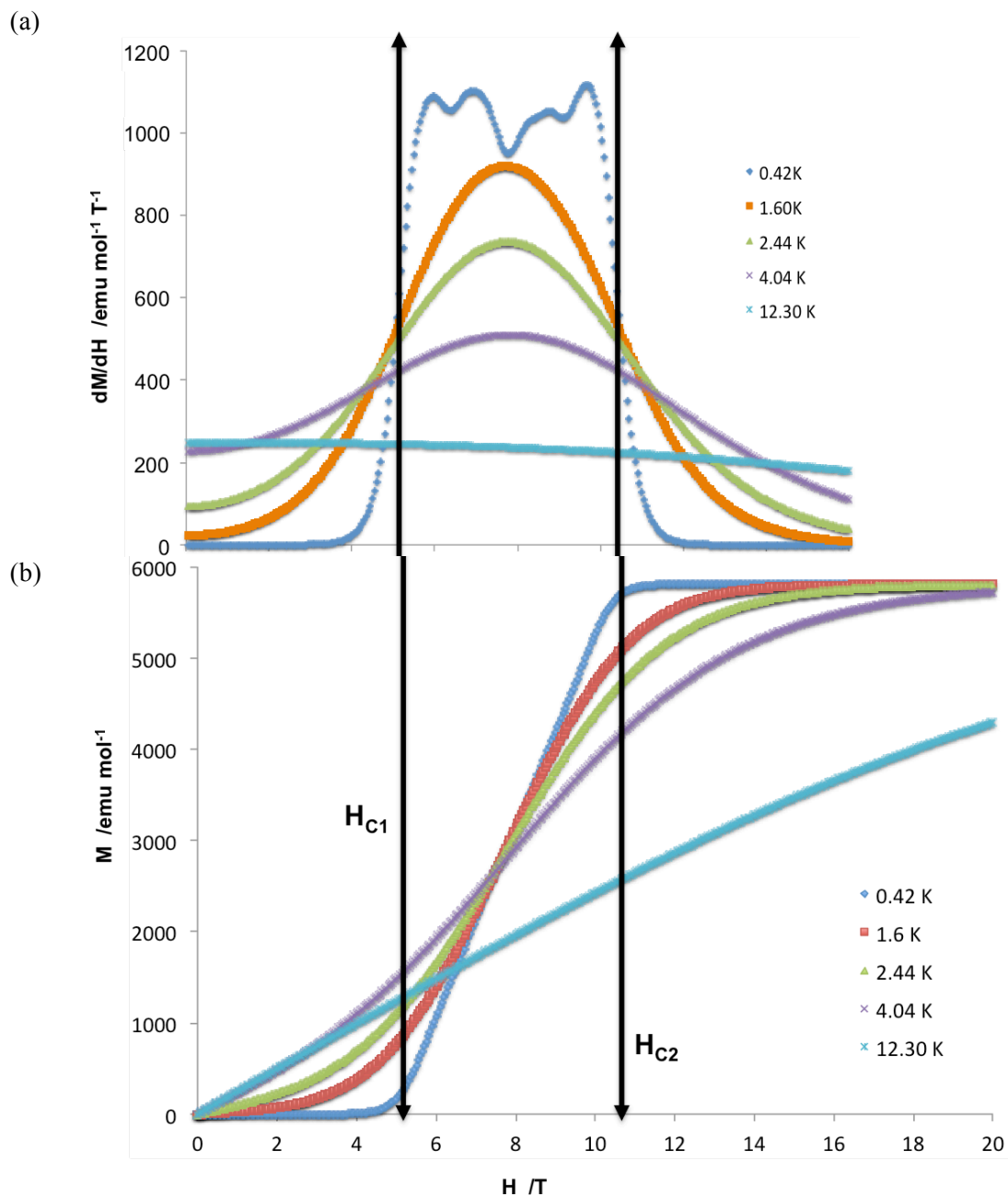


**Figure S6.1.** Calculated (a)  $dM/dH$  and (b)  $M(H)$  at 0.42, 1.60, 2.44, 4.04, and 12.30 K using the 3D magnetic topology and the  $J_{AB}$  values obtained by the tetramer approach at 4 K. See  $H_{c1}$  and  $H_{c2}$  coersive fields shown inset.

Direct comparison between calculated and experimental data of magnetization as a function of the reduced magnetic field,  $M/M_{\text{sat}}(H/\Delta)$  (see Figure S6.2), shows very good qualitative agreement. Note that  $M_{\text{sat}}$  and  $\Delta$  stand for the value of the magnetization once saturation has been reached and singlet-triplet spin gap, respectively. Also we must point out that the reduced definition of magnetic field, i.e.  $H/\Delta$ , has been used to compare our results to the experimental magnetization data, in line with Refs. [S6.1, S6.2]. Note that the experimental  $\Delta$  value is  $H_{c1,\text{exp}}$  which is 7.4 T. Although our results compare well with the experimental data and the appearance of three spin regimes is supported by the analysis of the magnetic wavefunction (see main text), it is a fact that our calculated data is shifted *ca.* 2.78 T towards lower magnetic fields, i.e.  $H_{c1} = 5.2$  T compared to  $H_{c1,\text{exp}} = 7.4$  T and  $H_{c2} = 10.4$  T compared to  $H_{c2,\text{exp}} = 13.2$  T.

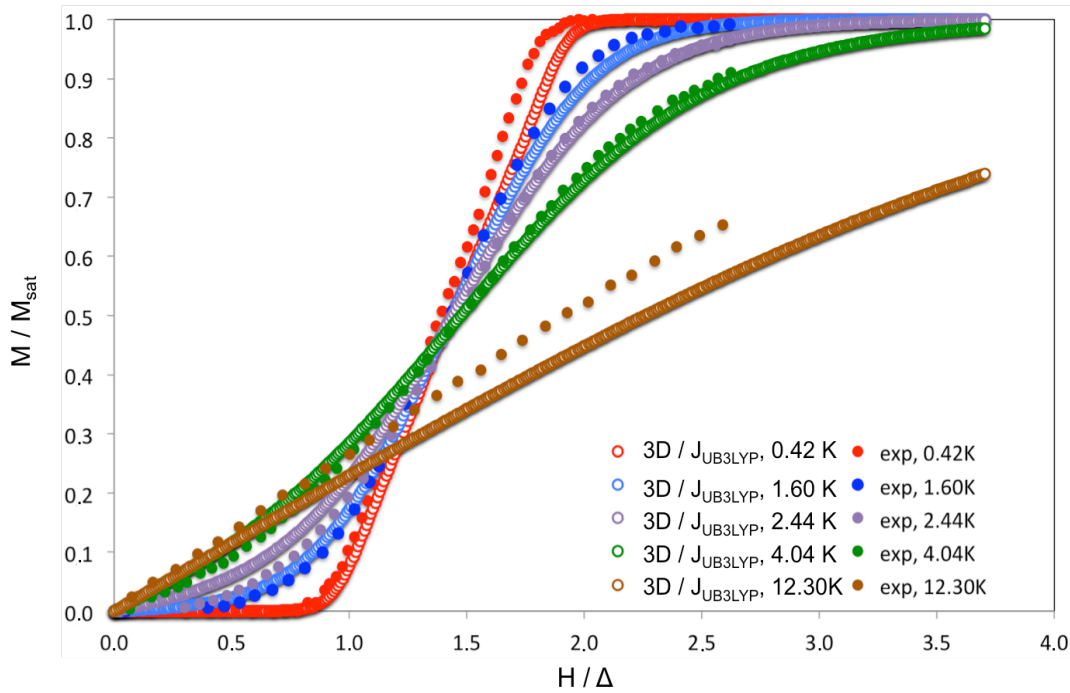


**Figure S6.2.** Raw calculated (empty colors) and experimental (filled symbols) data.

Re-analyzing our results using data from 4K and room temperature, we have realized why there is a shift between the experimental  $H_{c1}$  and  $H_{c2}$  values and ours. The reason turns out to be simpler than expected: the crystallographic data plays a non-innocent role in determining the values of the critical field. For some time now, we are aware of how important is to study the dependence of the magnetic topology on the temperature.<sup>[S6.3]</sup> Therefore, we always assess that dependence using all available crystallographic data (if it has been determined at different temperatures). For CuHpCl, we used two sets of crystallographic data at 4 K and at room temperature (RT). We concluded that the magnetic topology was hardly affected by the temperature, i.e. the magnitude of the  $J_{AB}$  magnetic exchange values were only slightly influenced by thermal contraction. Accordingly, all magnetic properties were calculated with the lowest temperature data set because the most interesting behavior of CuHpCl is observed *ca.* 0.42K. Unexpectedly, using the magnetic model with the  $J_{AB}$  couplings obtained at RT, the value of  $H_{c1}$  has a non-negligible dependence on the temperature at which the crystal structure of CuHpCl has been characterized (see Figure S6.3). Using calculated data at RT,  $H_{c1}$  is *ca.* 4.7

T, at 4 K is *ca.* 5.2 T and at 0.42 K (experimental) 7.4 T. The magnetic field range between  $H_{c1}$  and  $H_{c2}$  is also temperature dependent. It spans 4.7 T at RT, 5.2 T at 4 K and 5.8 T at 0.42 K. Therefore, if lower than 4 K crystal data was available, no doubt our estimated value of  $H_{c1}$  would be further improved. Also, in view of the high sensibility of  $H_{c1}$ , thermal fluctuations might play a role in fine tuning the estimated value of  $H_{c1}$ . Note that we did assume that thermal effects would not be important because we were working with CuHpCl crystallographic data at 4 K. Note also that the inclusion of thermal fluctuations is done by means of *ab initio* molecular dynamics (AIMD), which are out of the scope of this paper.

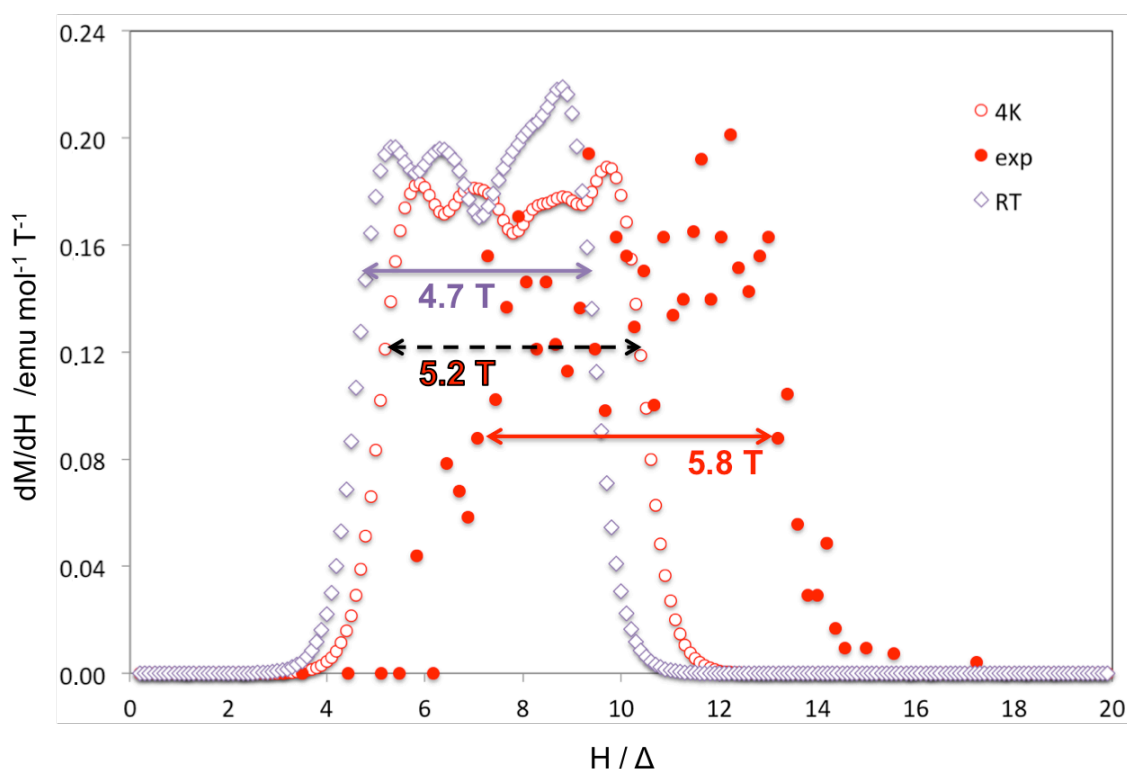


**Figure S6.3.** Comparison between experimental (red filled symbols) and calculated (empty symbols) using a 3D magnetic model parameterized with  $J_{AB}$  obtained at room temperature (RT, purple) and at 4K (red). The magnetic field span is also indicated numerically and qualitatively by an arrow.

[S6.1] X. Wang, and L. Yu, *Phys. Rev. Lett.*, 2000, **84**, 5399

[S6.2] C.A. Hayward, D. Poilblanc, and L.P. Levy, *Phys. Rev. B*, 1996, **54** R12 649

[S6.3] (a) M. Deumal et al. *Chem Eur J.* **2004**, 10, 6422; (b) M. Deumal et al. *Chem Eur J.* **2010**, 16, 2741.

## Supporting Information Section 7

We have recently disclosed<sup>[S7.1]</sup> that the heat capacity  $C_p(T)$  measures the energy variation due to the 3D propagation of the interaction of two magnetically connected spins, that is, to short-range ordering. In addition we have proposed the magnetic capacity,  $C_s(T)$ , as a measure of the thermal variation of the spin multiplicity of the system and, thus, reflects the importance of magnetically non-connected spin alignment and how the dominant effect of long-range spin correlation governs the magnetic behavior of molecule-based crystals (and in general of magnetic compounds). It was thus shown that the current definition of the critical temperature  $T_C$  for magnetic systems, which is associated with a maximum in the heat capacity  $C_p(T)$ , does not capture the magnetic nature of the system, because it excludes long-range magnetic order. Instead, a maximum in  $\partial[\chi T(T)]/\partial T$ , which is related to the magnetic capacity  $C_s(T)$ , that in turn includes changes in short- and long-range spin order/disorder, is a more broadly applicable definition of the magnetic transition temperature. It was also revealed that the analysis of the behavior of the critical temperature  $T_C$  of both magnetic  $C_s(T)$  and heat  $C_p(T)$  capacities provides information on the importance of long-range spin correlation.

For CuHpCl, we discover that  $T_C$  calculated from either  $C_p(T)$  or  $C_s(T)$  is nearly equal (see Figure S7.1), which we know it is the case only in those molecule-based systems in which either the long-range spin correlation can be neglected, or there is no 3D propagation of the spin coupling. Since we have determined that the magnetic topology of CuHpCl is 3D, we must conclude that the long-range spin correlation is not significant.

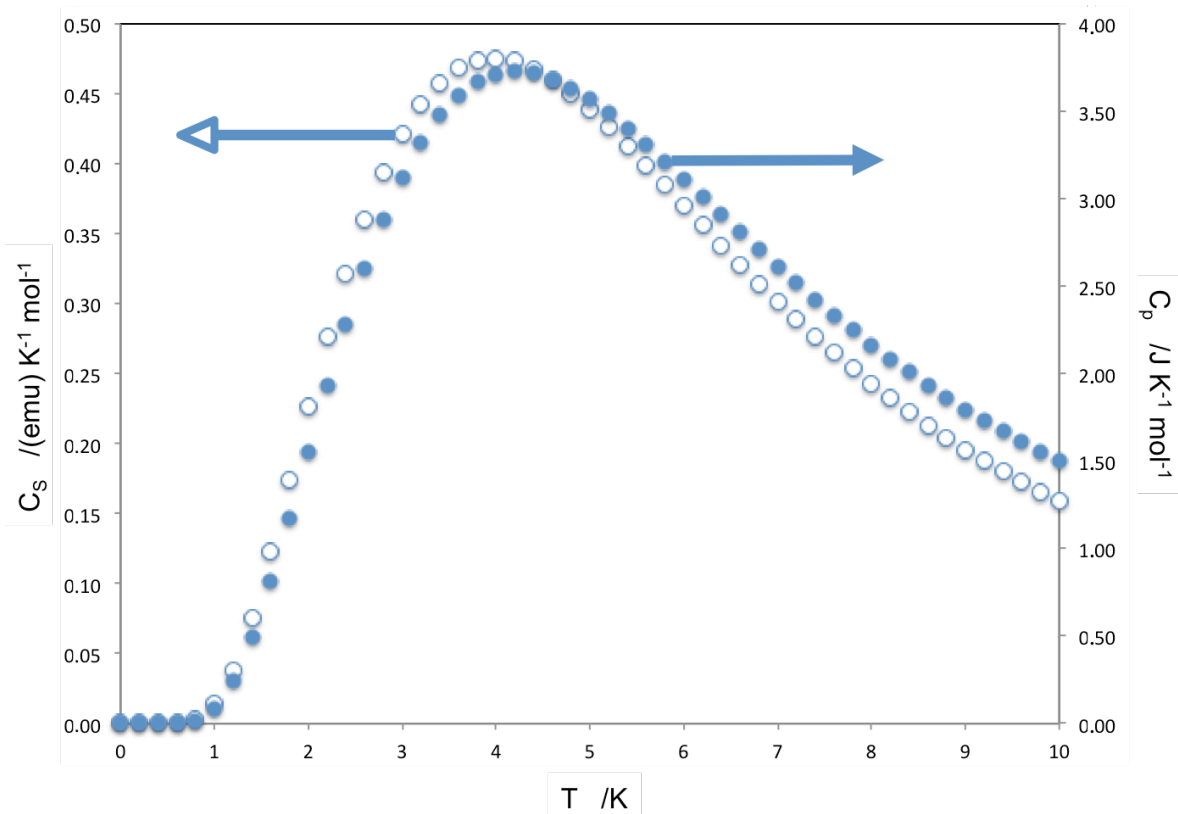


**Figure S7.1.** Calculated heat capacity  $C_p(T)$  (right axis) and magnetic capacity  $C_s(T)$  (left axis) for CuHpCl molecule-based system.

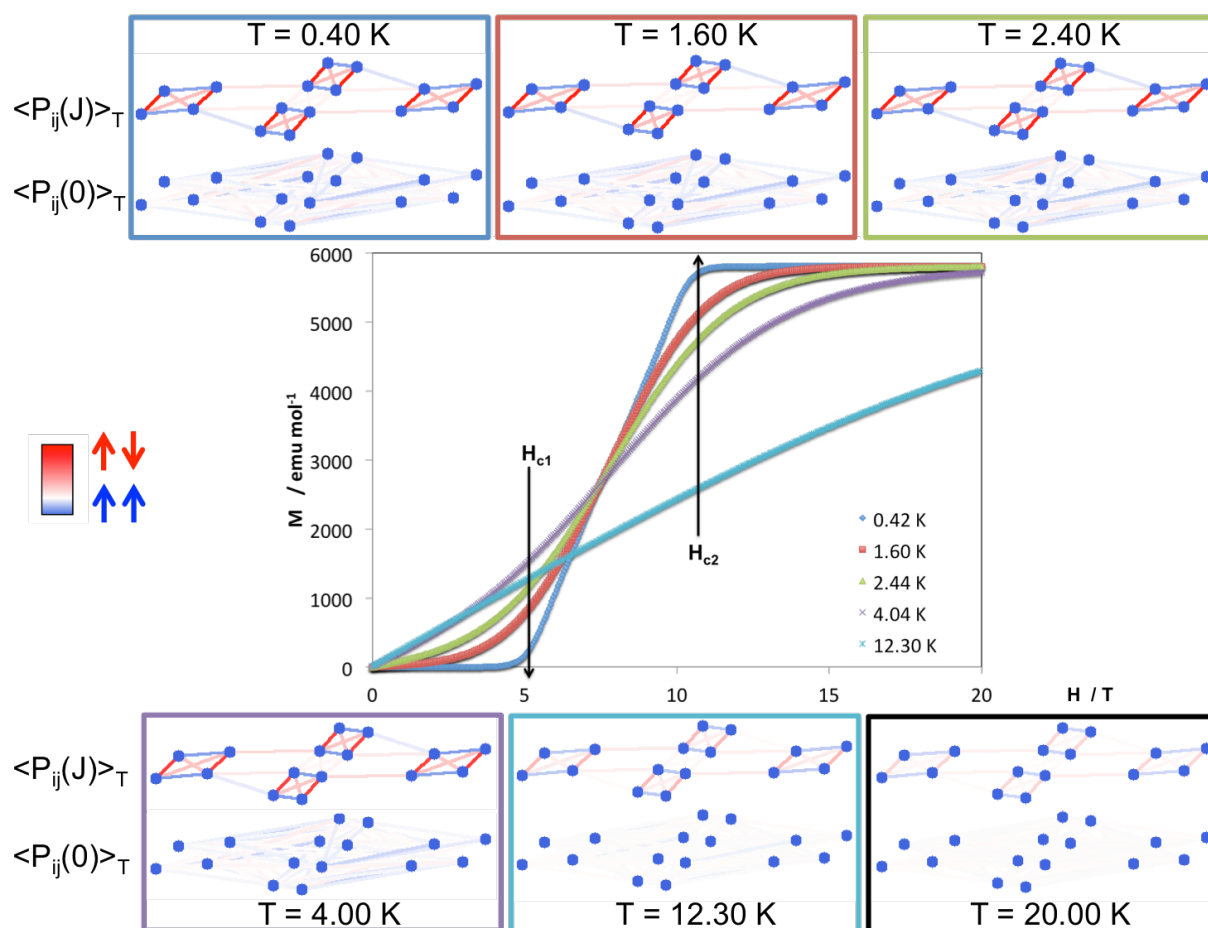


**Figure S7.2.** Temperature dependence of the magnetic correlation between all spin units at 0.40, 1.60, 2.40, 4.00, 12.30 and 20.00 K (in accordance to the magnetization experimental data).  $\langle P_{ij}(J) \rangle_T$  and  $\langle P_{ij}(0) \rangle_T$  refer to short-range and long-range spin correlation between magnetic units, respectively. Notice that spins coupled are represented in red, and spins arranged parallel in blue. Note also that the thickness of the lines connecting radicals is proportional to the strength of the correlation between spins.

The magnetic capacity  $C_s(T)$  is also useful because it can be interpreted in terms of the molecular structure of the crystal using the magnetic wavefunction for each magnetic microstate. For this interpretation, we have used a Valence Bond analysis of the magnetic wavefunction. This analysis provides information about the spin correlation between magnetic units, and enables to visualize the temperature dependence of the magnetic correlation between all spin units.

We have performed this analysis at different temperatures in accordance to the magnetization experiments. Therefore, the short-range and long-range spin correlation between magnetic units (see  $\langle P_{ij}(J) \rangle_T$  and  $\langle P_{ij}(0) \rangle_T$ , respectively, in Figure S7.2) has been studied at 0.40 K, 1.60 K, 2.40 K, 4.00 K, 12.30 K and 20.00 K. Clearly, the largest contribution from long-range spin correlation comes from the lowest 0.40 K temperature, being practically zero both short- and long-range ordering at 20.00 K. It follows that for CuHpCl even at the lowest temperature the short-range magnetic correlation is the only meaningful contribution. It can thus be concluded that the long-range spin correlation can be neglected, which was also inferred from comparison between critical temperatures calculated from heat and magnetic capacities.

**Table S7.1.** Information regarding the ten lowest energy spin states extracted from the 3D magnetic model space (16 radical model shown inset in Figure S7.2); namely the state number and corresponding spin multiplicity (state #, S), and the normalized Boltzmann population at six different temperatures (0.40 K, 1.60 K, 2.40 K, 4.00 K, 12.30 K and 20.00 K)

T /K	State #, S										Total %
	1, S=0	2, S=1	3, S=1	4, S=1	5, S=1	6, S=1	7, S=1	8, S=0	9, S=1	10, S=2	
0.40	100.0	0	0	0	0	0	0	0	0	0	100
1.60	95.0	2.5	1.3	0.08	0.07	0.03	0.02	0	0.01	0.02	98.4
2.40	72.0	9.3	5.8	4.3	3.8	0.45	0.36	0.10	0.29	0.47	95.1
4.00	24.0	11.0	8.2	6.7	6.4	1.8	1.6	0.47	1.4	2.2	63.7
12.30	0.21	0.34	0.31	0.29	0.28	0.19	0.18	0.06	0.17	0.29	2.3
20.00	0.04	0.08	0.08	0.08	0.07	0.06	0.06	0.02	0.05	0.09	0.6

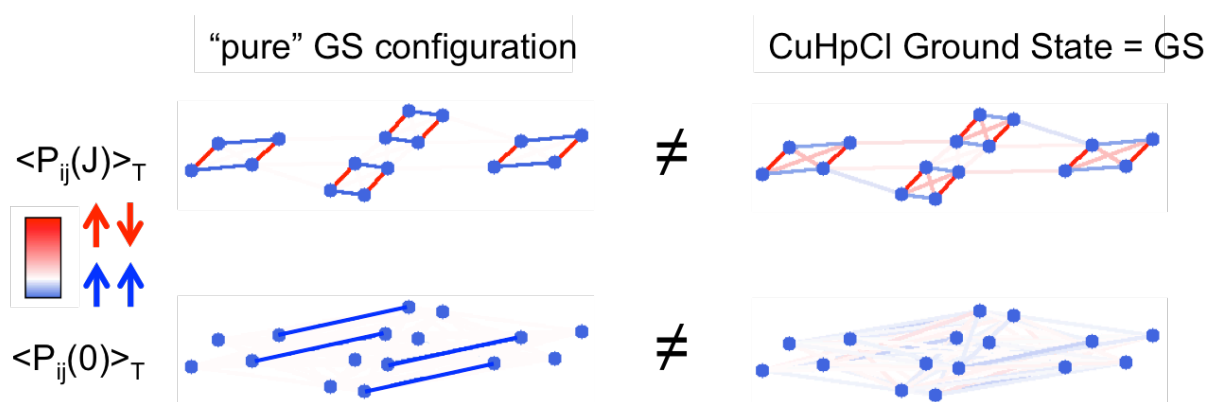


**Figure S7.3.** Short-range  $\langle P_{ij}(J) \rangle_T$  and long-range  $\langle P_{ij}(0) \rangle_T$  spin correlations for pure singlet ground state GS configuration (left) and CuHpCl ground state GS configuration (right). Notice that spins coupled are represented in red, and spins arranged parallel in blue.

It is also interesting to analyze the distribution of the Boltzmann population (see Table S7.1). As expected, at 0.40 K the only populated state is the singlet ground state (GS).<sup>[S7.2]</sup> Below 2.4K, in addition to the singlet GS, there are four excited states of triplet spin multiplicity that also contribute to describe the behavior of CuHpCl. Strikingly, while at 4.00 K the first ten states carry 64% of the population, at 12.30 K these very same ten states only carry a 2.3% of the total Boltzmann population.

Finally, comparison between the short-range  $\langle P_{ij}(J) \rangle_T$  and long-range  $\langle P_{ij}(0) \rangle_T$  spin correlations of a pure singlet AFM ground state and the CuHpCl ground state shows that in our case the singlet ground state is the collective result of singlet as well as higher multiplicity configurations (see Figure S7.3).

[S7.1] J. Jornet-Somoza, M. Deumal, J. Borge, and M.A. Robb, *J. Phys. Chem. A*, 2018, **122**, 2168,

[S7.2] The number of spin states comes from the full diagonalization of the magnetic model made of N radicals. Note that the magnetic model must be constructed to reproduce the magnetic topology of the molecular crystal. Therefore, there are  $N! / [(N/2)! (N/2)!]$  spin states. Our 3D magnetic model consists of 16 radicals. Therefore, there are 12870 spin states of spin multiplicity ranging from S=0 to S=8. Table S7.1 only shows the ten lowest energy spin states.